Flux surface identification by spatio-temporal coupling with partial mutual information analysis of electron cyclotron emission data

J F Guerrero Arnaiz[1,2], **A Dinklage**[1,2], **B Pompe**[2], **J Geiger**[1], **M Hirsch**[1], **U Höfel**[1],
N Marushchenko[1], **Y Turkin**[1], **R C Wolf**[1] **and the W7-X Team**

[1] Max-Planck-Institut für Plasmaphysik, Greifswald, Germany
[2] Universität Greifswald, Institut für Physik, Greifswald, Germany

E-mail: juan.fernando.guerrero.arnaiz@ipp.mpg.de

Abstract

Fluctuations of electron cyclotron emission (ECE) signals are analyzed for differently heated Wendelstein 7-X plasmas. The fluctuations appear to travel predominantly on flux surfaces and are used as 'tracers' in multivariate time series. Different statistical techniques are assessed to reveal the coupling and information entropy-based coupling analysis are conducted. All these techniques provide evidence that the fluctuation analysis allows one to check the consistency of magneto-hydrodynamic (MHD) equilibrium calculations. Expanding the suite of techniques applied in fusion data analysis, partial mutual information (PMI) analysis is introduced. PMI generalizes traditional partial correlation (Frenzel and Pompe *Phys. Rev. Lett.* **99** 204101) and also Schreiber's transfer entropy (Schreiber 2000 *Phys. Rev. Lett.* **85** 461). The main additional capability of PMI is to allow one to discount for specific spurious data. Since PMI analysis allows one to study the effect of common drivers, the influence of the electron cyclotron resonance heating on the mutual dependencies of simultaneous ECE measurements was assessed. Additionally, MHD mode activity was found to be coupled in a limited volume in the plasma core for different plasmas. The study reveals an experimental test for equilibrium calculations and ECE radiation transport.

Keywords: partial mutual information, electron cyclotron emission, magneto-hydrodynamic equilibrium, correlation analysis, stellarator, Wendelstein 7-X

(Some figures may appear in colour only in the online journal)

1. Introduction

Wendelstein 7-X (W7-X) is an *optimized*, superconducting stellarator [1–3]. The main goal of W7-X is demonstrating optimized stellarators to be an economic option for a fusion power plant. The notion of *optimization* in the context of stellarator research refers to the intentional shaping of the magnetic field. To this end, 3D shaped coils generate toroidal flux surfaces to meet with seven physical *optimization criteria* [4]. The optimization criteria of W7-X address potential show-stoppers of classical stellarators, namely to reduce particle and energy losses of both the thermal plasma and fast (fusion-born-like) particles as well as stability to achieve magneto-hydrodynamic (MHD) equilibrium at high plasma beta and (reactor-like) low collisionalities. Thus, the magnetic

equilibrium is one key to enjoy the benefits of the magnetic field optimization.

The experimental demonstration of *optimized* magnetic field geometry motivates strong interest in techniques that validate precalculated equilibria. The vacuum field has been demonstrated to meet with high accuracy requirements [5] and delivers—as one of the key benefits of stellarator fields—even at vanishing plasma beta confinement by nested flux surfaces. Since W7-X is equipped with superconducting coils, the field can be maintained at quasi steady-state (limited by the infrastructure up to 30 min). Ultimately, insight into the magnetic field geometry with plasma (at finite beta values) provides a next-step validation of field optimization. A specific question addressed in this paper provides indications for flux surfaces. Our technique traces plasma fluctuations simultaneously observed in electron cyclotron emission (ECE) emissivity time series on the inboard and outboard side of W7-X plasmas. The partial mutual information (PMI) technique benefits from the increase of significance levels and from capabilities to suppress spurious nonphysical signal contributions. PMI provides measures estimating how much two time series are related. The method has been developed from information theory [6] and we will show that it offers approaches to address shortcomings from traditional statistical time series analysis.

Conditional mutual information (PMI resp. transfer entropy (TE)) have been applied in very different fields. Examples are in medicine [7] (multichannel electroencephalographic recordings) and climatology (air-temperature anomalies at sea surface toward the upper troposphere) [8]. This paper, however, reports the first application of PMI in fusion data analysis extending early applications of TE [9]. To supplement MHD equilibrium reconstructions, the results are compared to independent flux surface mapping of the electron cyclotron emissivity. The comparison shows good agreement and delivers—beyond the validation aspect—confirmation of radiative transport. New insights could be retrieved applying concepts from information theory to determine *information entropies*. Differently to specific statistical moments (such as in correlation analyses), the information measures provide an overall measure of how much new data X_0 can be predicted from measurements $X_1, X_2, \ldots$. The complexity of the (chaotic) dynamics in a plasma as well as spurious contributions in the analyzed real-world data gives rise to limitations. In literature, practical limitations have been reported (see e.g. [10, 11]). In fusion, tools from information theory for coupling analysis were applied to high-sampled high temperature plasma data. Examples use Schreiber's TE [12]. Specific applications are the successful and fast detection of edge-localized modes [13]. A different example links coupling analysis to heat transport [9, 14, 15]. Limitations both in sensitivity and time-resolution, however, are to be expected in any technique. Clear limitations arise from instruments due to cross-talk, ambient noise (*smog*) and noise in highly sensitive detectors. That is, for real-world plasma data, co-information from sources beyond the measured data and dynamical noise affect the measurements. Thus, clearing coupling analysis from spurious dues is key to critically assess the causality reflected from spatio-temporal signals.

The TE technique makes an important step to address the aforementioned shortcomings. Assuming that an additional time series Y picks up spurious effects as well as the reference times serie X, TE discounts for those spurious signal contributions that both time series experience. TE thus delivers additional information not contained as 'underlying' spurious contribution and thereby significantly increases the significance of coupling measures between X and Y. The technique in this paper significantly extends TE by discounting additional signals: if sources of spurious contributions can be identified (e.g. in this paper it is the effect of electron cyclotron resonance heating (ECRH) on ECE measurements), a common driver or noise source in X and Y can be specifically discounted for. This results in an additional increase of significance levels which is shown to be prerequisite for the validation technique in this paper.

The paper is structured as follows: first, in order to assess how much different formulations of information entropies provide new insights, we briefly revise the background of PMI. Next, the description of the instrument (multi-channel ECE radiometer) focuses on the later application for the identification of flux surfaces. Then, the experimental technique is described to introduce the analysis approach. Afterwards, the results from the analysis of multivariate time series from discharges in W7-X provide the central part of this paper. Finally, conclusions will be drawn along a discussion of the different approaches, section 4.

2. Measuring coupling in multivariate time series

The concepts of information flow and transport appear to be closely related. Self-reproducing, open thermodynamical system fed by matter and energy may maximize a process quantity termed *entropy* [16], which is related to the number of states that the system can adopt and, therefore, to the amount of *information* that can be stored or transmitted by it [17]. Heat transport carried by turbulent plasma flows obeys the second principle and the entropy production rate defines the causality of turbulent flows [18]. Both views reflect entropy to be the directing entity for the causality of processes, thus suggesting that an estimate of information flows from experimental data could deliver insight into transport processes. This paper addresses the extent to which different techniques may be employed in order to conduct such measurements. Here, we will apply linear correlation, mutual information (MI) and PMI analysis on time series retrieved through a heterodyne multichannel electron cyclotron radiometer. The latter methods rely on Shannon's information theory [19] and their outcome is considered to estimate the coupling in terms of common (mutual) information of different observables. In general, we would expect that the sum of the thermodynamic entropies of two systems is strictly less than the thermodynamic entropy of the joint system, if there are statistical dependencies between the observables.

An indicator of the strength of the linear association between two variables or time series is given by the Pearson product-moment correlation (PPMC) [20], for which a line of best fit is drawn across the data such that the agreement

between the fit and the data can be expressed as a coefficient r. Correlation coefficient $|r| = 1$ means that there is a deterministic linear relation between the time series, i.e. $y_t = a + bx_t$ with some fixed real values a and b. More precisely,

$$r = \pm 1 \quad \Leftrightarrow \quad \frac{y_t - \bar{y}}{\sigma_y} = \pm \frac{x_t - \bar{x}}{\sigma_x}$$

holds for each t, with standard deviations σ_x and σ_y and means $\bar{x}$ and $\bar{y}$ of series x and y, respectively. Moreover,

$r = 0 \quad \Leftrightarrow \quad$ 'x and y are not correlated (linearly dependent)'

$r = 0 \quad \not\Rightarrow \quad$ 'x and y are statistically independent'

$r = 0 \quad \Rightarrow \quad$ 'x and y might be nonlinearly dependent'.

One step further, the linear correlation analysis can be performed as a function of the time displacement between samples by shifting one of them by a number of time steps relative to the other which results in the cross-correlation function.

Since details and mathematical background of the information theoretic methods is found in literature [6, 12], only a pictorial explanation is given here to explain why the PMI is capable to discount for perturbations. MI and PMI are information measures based on the concept of Shannon entropy H of a probability distribution $\{p_j\}$ of a random variable X,

$$H(X) = -\sum_j p_j \mathsf{ld}(p_j).$$

We use dual logarithm $\mathsf{ld} \equiv \log_2$, hence entropy is measured in *bit* (Binary digit) representing the answers of optimal 'yes-no' questions. H represents an average of $\mathsf{ld}(1/p_j)$ w.r.t. the probability distribution $\{p_j\}$. It is interpreted as the (mean) *a priori uncertainty* on X before measurement, or as the posterior information on X gained due to a measurement.

Consider now another random variable Y with probability distribution $\{q_k\}$. If there are statistical relation between X and Y, a measurement of the latter yields some information on X. Hence, starting with the uncertainty $H(X)$ there remains the uncertainty $H(X|Y)$ on X due to the measurement of Y. Consider now the joint distribution $\{s_{jk}\}$ of the random vector (X, Y), then the (mean) conditional uncertainty is obtained from the corresponding conditional probabilities $p_{j|k} = s_{jk}/q_k$,

$$\begin{aligned} H(X|Y) &= \sum_k q_k \left(-\sum_j p_{j|k} \mathsf{ld} p_{j|k} \right) \\ &= -\sum_{j,k} s_{jk}(\mathsf{ld} s_{jk} - \mathsf{ld} q_k) \\ &= H(X, Y) - H(Y). \end{aligned}$$

If we subtract from the *a priori* uncertainty $H(X)$ on X the posterior uncertainty on X due to measuring Y, we get the information on X contained in Y,

$$\begin{aligned} I(X, Y) &= H(X) - H(X|Y) \\ &= H(X) + H(Y) - H(X, Y). \end{aligned}$$

It is called *mutual information* because it is symmetric, $I(X, Y) = I(Y, X)$. In general, $0 \leq I(Y, X) \leq \min\{H(X), H(Y)\}$. We get $I(X, Y) = 0$ if and only if X and Y are statistically independent, i.e. iff $s_{jk} = p_j q_k$ for all j, k. If $I(Y, X) = H(X)$ then X is a function of Y. We note that there are also other quantities measuring or detecting dependencies like contingency, however, entropy measures have a more profound interpretation in coding theory.

PMI extends MI, allowing one to discount for a third random variable Z. For that purpose, we consider the random vector (X, Y, Z) with joint distribution $\{s_{jkl}\}$. PMI is defined as

$$I(X, Y|Z) \equiv I(X, (Y, Z)) - I(X, Z).$$

It can be rewritten as,

$$\begin{aligned} I(X, Y|Z) &= H(X|Z) - H(X|(Y, Z)) \\ &= H(X, Y) + H(Y, Z) - H(Z) - H(X, Y, Z) \\ &= \sum_{jkl} s_{jkl} \mathsf{ld} \frac{s_{jkl} \cdot s_{\bullet\bullet l}}{s_{j\bullet l} \cdot s_{\bullet kl}}. \end{aligned}$$

Here we use the marginal distributions $s_{\bullet\bullet l} \equiv \sum_{jk} s_{jkl}$, $s_{j\bullet l} \equiv \sum_k s_{jkl}$, and $s_{\bullet kl} \equiv \sum_j s_{jkl}$. Note that PMI is symmetric w.r.t. an exchange of X and Y $I(X, Y|Z) \neq I(Y, X|Z)$ as well,

$$I(X, Y|Z) = I(Y, X|Z).$$

Conditioning the MI of X and Y on Z, makes PMI analysis a tool to investigate causalities, since the effect of common drivers Z on two apparently coupled time series can be measured. Somewhat differently worded, PMI measures what one random variables Y tells us about another one X (in terms of MI) without the information from a third random variable Z. For our application, we use the estimator proposed in [6] based on a kth-nearest-neighbor algorithm.

The TE $T_{Y \to X}$ introduced by Schreiber [12] estimates common information of two time series $\{X_n\}$ and $\{Y_n\}$ (the latter shifted by a delay) conditional on time shifted measurements of the time series under consideration $\{X_n\}$:

$$T_{Y \to X} = I(X_{n+1}, Y_{n-k}|X_{n-k}).$$

In other words, $T_{Y \to X}$ measures the information in Y_{n-k} on X_{n+1} that is not in X_{n-k}.

3. Multivariate ECE measurements on W7-X for the detection of flux surfaces

Figure 1 shows aspects of the magnetic field geometry of W7-X. The field is mainly generated by 50 nonplanar and 10 planar coils of seven different types (not shown in figure 1). Each type can be charged separately allowing one to change the field topology. The mean major radius of the torus is $R = 5.5$ m. With an aspect ratio of about ten, a typical plasma volume of about 30 m^3 is generated.

A view from the top (figure 1(a)) shows the five-fold symmetry of W7-X. The field strength (mod B) is seen to vary on the flux surfaces giving rise to field ripples. Particles traveling along the field lines therefore experience different magnetic
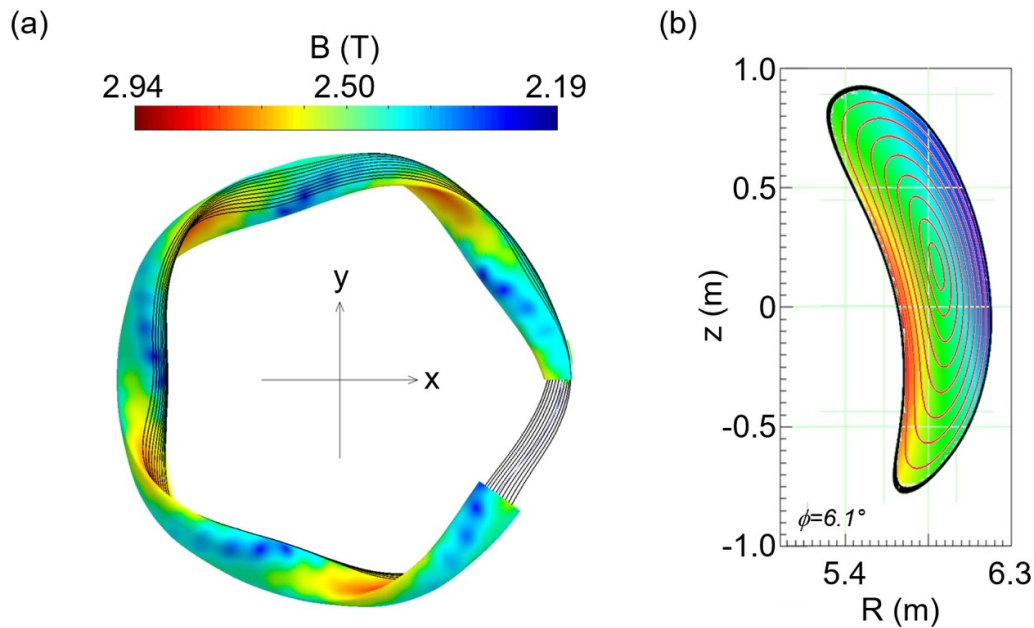
Figure 1. (a) Shows a 3D view on the last closed flux surface of the W7-X standard island-divertor configuration (no islands shown) the open section provides the magnetic axis. The color corresponds to mod B and the black lines indicate a field line. (b) shows a poloidal cross section in the toroidal plane of ECE radiometer measurements. The background color show mod B behind a representative set of flux surface cross sections. Figures are produced with mcviewer based on MConf library, see [21].

mirrors giving rise to locally trapped particles. The pentagonal shape of the torus has high fields on the inboard side in regions of highest curvatures ('corners'). In the straight sections, there is less field variation along the major radius R. With this background, W7-X is said to have a linked-mirror configuration. The field structure forces trapped particles (in the long mean free path) to precess poloidally in the straight sections and to be reflected from the high field regions at high curvature. It is the precession of deeply trapped particles in the straight sections that diminishes convective losses by grad-B and curvature drifts. Since those losses are much smaller than in classical stellarators, W7-X is *drift optimized*.

Dependent on the magnetic configuration (that can be changed), one finds poloidal cross sections with large variations of mod B. Figure 1(b) shows the cross section observed by the ECE radiometer allowing lines of sight with large variation of mod B and thereby the gyrofrequency. Figure 1(b) also indicates flux surfaces which are considered to be surfaces of constant pressure in ideal MHD. It is directly seen that mod B is different for inboard and outboard sides of an individual flux surface. Any fluctuation of the electron pressure will be quickly leveled off on the flux surface. Thus, coupling analysis of fluctuating plasma parameters are expected to be capable of identifying the flux surface position in the opposite field side of a spatial plasma parameter measurement such as the electron temperature T_e.
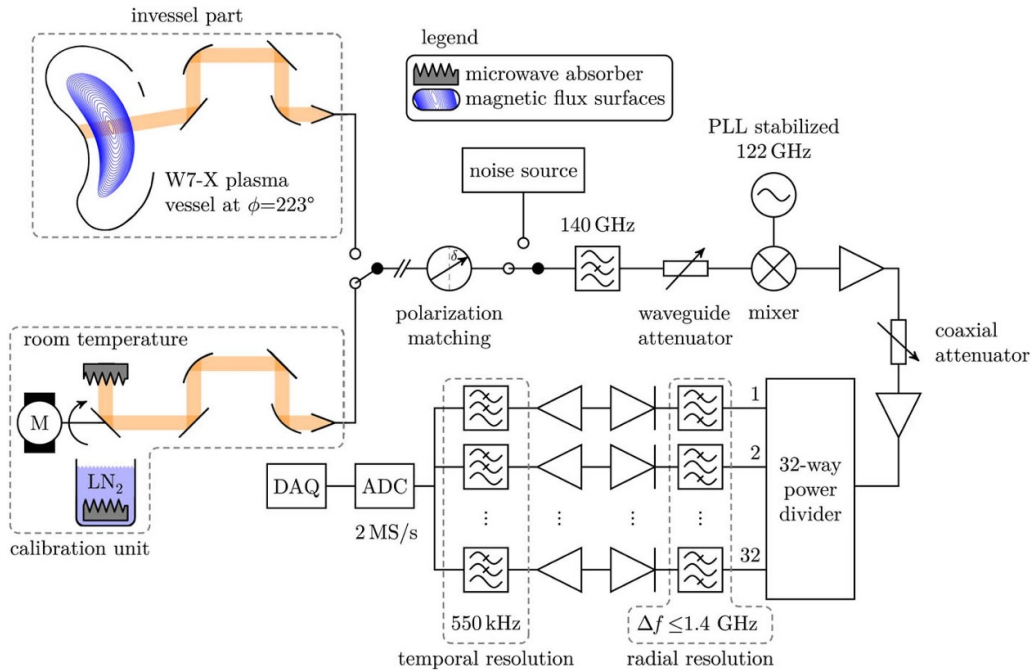
3.1. ECE radiometer at W7-X

Electron cyclotron emission radiometry is well established on stellarators [22]. The intensity of ECE due to the gyromotion of the electrons provides a measure for T_e. If ECE is measured with radiometers (delivering intensities in finite frequency windows), spatio-temporally resolved electron temperatures can be inferred. Since ECE radiometers provide highly sampled signals, they enable beyond the derivation of electron (radiation) temperature profiles also the detection and analysis of temperature perturbations. However, fluctuations of the measured signals do not necessarily imply perturbations in plasma temperature, but may be due to, e.g. system noise.

The ECE diagnostic on W7-X measures in the microwave range with a 32-channel heterodyne radiometer [22–24]. The principal set-up is shown in figure 2. The instrument measures continuously the second harmonic X-mode emission between 124 and 162 GHz at 2.5 T, allowing one to derive T_e profiles. For each ECE channel, the detected microwave intensity is absolutely calibrated by comparison with the emission of a blackbody source. The calibration measurement consists of the detection of radiation from surfaces at two well-defined temperatures (room temperature and boiling temperature of liquid nitrogen). The radiation collected by an observation optics is received by a microwave horn antenna and led by waveguides to the receiver system outside the torus hall. The radiation has to pass through a notch filter, required to suppress spurious microwave radiation from high power electron cyclotron heating. Here, the gyrotrons emit frequencies matching with the second harmonic gyrofrequency at the plasma center at the toroidal position of heating ($\approx$140 GHz). The ECE channels are enumerated from #1–32, where the higher the enumeration, the higher the frequency at which the measurements are performed. For the subsequent discussion, the ECE channel #16, which detects the ECE at $\approx$139 GHz, is at the edge of the notch filter characteristic and will be referred to as the *heating*

Figure 2. Signal path of the multichannel broadband heterodyne radiometer at W7-X: from plasma and calibration source to DAQ. Adapted from [23].

channel. ECE channels $\#1-15$ measure the low-field side and channels $\#17-32$ the high-field side. The microwaves are detected and down-converted to lower frequencies $(4-40\,\text{GHz})$ via a stabilized local oscillator at $122\,\text{GHz}$. Then, the down converted signals are split into 32 channels and bandpass filtered with bandwidths of $0.25\,\text{GHz} \leq \Delta f \leq 1.4\,\text{GHz}$. After predetection amplifiers, detection diodes and a low-pass filter to avoid aliasing, a $16\,bit$ analog-to-digital converter with a sampling frequency of up to $2\,\text{MHz}$ converts the intensities into sampled time series. Finally, the fast sampled digital signals arrive in the data acquisition system (DAQ), resulting in a diagnostic with spatial and temporal resolutions of the order of 1 cm and $10\,\mu s$ [25]. The details of the set-up are relevant to assess measurement noise and common drifts that may affect groups or individual of channels of the radiometer.

According to the previous discussion, a spatial profile of T_e can be derived from calibrated spectral intensities and the assignment of frequencies to mod B. The latter assignment is made by calculating the field with a 3D MHD equilibrium code (VMEC (variational moments equilibrium code) [26]) that solves the force balance of ideal MHD under the assumption of the existence of flux surfaces. This approach is employing the cold resonance of ECE, assuming that the measured intensity is emitted from the location where the probed frequency corresponds directly to the cyclotron frequency. The cold resonance model is valid for a single emitting electron only. Radiation transport in a plasma including reabsorption and -emission by electrons must be taken into account to explain the finite optical thickness and hence the layer where the measured radiation stems from. For conditions in the plasma core, this optical thickness is sufficient to be treated as blackbody radiation from a finite layer right at somewhat higher field than that of the cold resonance location. The code TRAVIS

(TRAcing VISualized) [21] solves the radiative transport and the radiative transfer equations using the 3D magnetic equilibrium and 3D ray-tracing. The correction of radiative transport results in spatio-temporal radiation temperature measurements and profiles as shown later in figures 3 and 4 respectively.

3.2. ECE time series from W7-X and coupling analysis

Figure 3(a) shows waveforms analyzed in this paper. The discharge (20160309.22) was conducted in the first experimental campaign of W7-X which allowed (due to unprotected walls) small heating energies only. The plasma was heated by electron cyclotron heating and the power (figure 3(a) red line) was applied for one second at different heating power levels for 300 ms each (after a 100 ms start-up phase), resulting in time periods with a 'high' heating power of $2\,\text{MW}$, 'mid' power of $1.3\,\text{MW}$ and 'low' of $0.6\,\text{MW}$. Within the achievable density in the respective plasma campaign, the plasma density was relatively low $(<1.2 \times 10^{19}\,\text{m}^{-3})$. These conditions reveal so called core electron-root confinement, a confinement regime typically exhibiting regions of large positive radial electric fields in the core. The reason lies in (parameter dependent) non-intrinsically ambipolar electron and ion fluxes (in stellarators) [27]. With its large spatial T_e variations, the chosen discharge provides a cross section of different plasma regimes relevant to assessments of the optimization criteria in W7-X [28] with large and small prevailing neoclassical electron energy transport. The response in T_e is shown in figure 3(a) as well. Different channels of the radiometer indicate electron temperatures as high as $T_e \sim 6\ldots 8\,\text{keV}$ in the center (channel #12 and #18) and much lower temperature in the periphery of the plasma. The transition of the ECE channel waveform due to changes

(a)   (b)
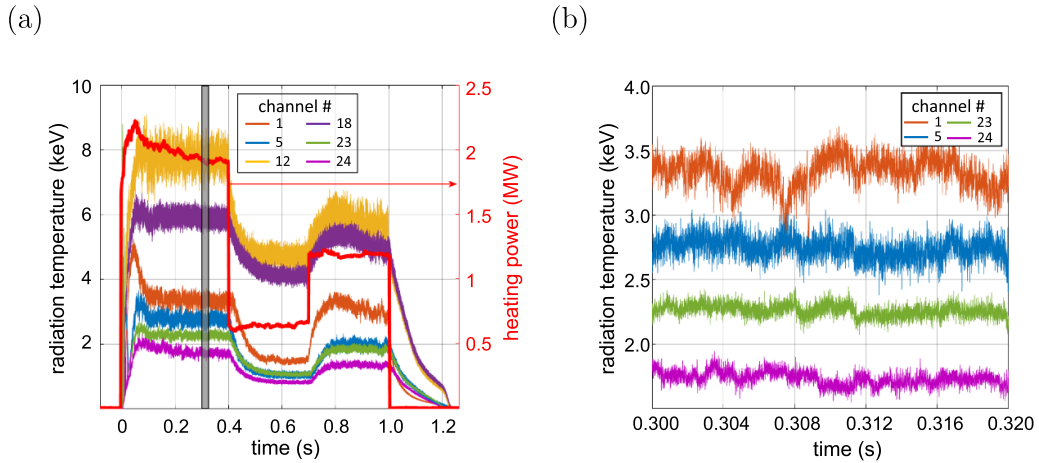
Figure 3. Overview plot of relevant plasma parameters for the flux surface identification. (a) Electron temperature T_e at various radial positions obtained through the ECE diagnostic and the power of the main plasma heating source (red line). The gray shaded area indicates the time interval selected to analyze the ECE time series. This interval is magnified in (b).

of the heating power reflects local changes of the energy confinement.

Figure 3(b) shows a magnification of selected ECE time series from four radiometer channels indicated by the channel number. The ECE time series were chosen in a stationary time window from $t = 0.300\ldots0.320$ s. Visual inspection reveals apparent similarities in the time series. E.g. a pulse-like structure is found both in channels #23 and #5 at around 0.317 s. It is noted, however, that many of the excursions beyond the apparent noise level are difficult to identify in other channels. All signals show noise levels which may vary from channel to channel. This simple observation already indicates that the observed fluctuations of the signals may result partly from the instrument. Dynamical noise (from the plasma), however, is not excluded and it will be shown later that this part of the signal contains 'tracer fluctuations' that appear to be detectable by the information entropies. This ambiguity is sought to be addressed by the PMI analysis below. In order to estimate the statistical significance of the information measures, the coupling between one random noise signal of the same duration as the ECE time series and other hundred equally generated signals are analyzed through the MI, PMI and TE methods. This results in a significance threshold level of 8×10^{-3} bit.

The set-up of the ECE indicated ECE channels close to the heating frequencies to be affected by large spurious 'stray-radiation'. Given the capabilities of PMI to discern the information of a third source from the MI of two others, PMI analysis will be applied in this case to discount the information coming from an ECE channel that is heavily directly influenced by the plasma heating source. In the remainder we present analyses for the quasi-stationary signals in the 'high' power region.

Since we address spatial coupling revealed by the radiometer channels, we need to address where the detected emissivity in each channel is born. With lines of sight measured in real space geometry and measurements of the coil positions, coordinate transforms are conducted to assign positions to flux surfaces. While a first approximation of the

emissivity position is given by the electron cyclotron resonance frequency, resonance broadening and radiation transport is considered in the ray-tracing calculations with the code TRAVIS. The broadening is mainly relativistic since the line of sight of the radiometer is almost perpendicular to the guiding center and, therefore, Doppler broadening is negligible. The radiation transport needs to be considered since the assumption of equal emission and absorption (blackbody) is gradually violated as the plasma becomes optically gray (at lower temperatures). The bar in the abscissa in figure 4 indicates the dominating regions (spatial width) the emissivity is emerging from (5%–95% interval). These regions are asymmetric in the low-field side near the edge (where the optical depth is low) due to a relatively large amount of radiation coming from the plasma core, but less from the edges themselves. This asymmetry is also observed in the high-field side and is in the same direction given the sign change of the T_e gradient. Since the radiation transport depends on densities and temperatures, the TRAVIS calculation refers to the time interval of the coupling investigation.

The contributions to the ECE mostly come from waves with a polarization perpendicular to the background magnetic field given by the oscillating E-field (X-mode), thus the radial position of the measurements to be considered for the following coupling analysis will be those from the X-mode. Negative values of the effective plasma radius ρ (defined as $\rho = \frac{r}{a}$, where $\frac{r}{a}$ is the normalized minor radius of the plasma) represent radial regions near the high-field side positions with respect to the axis. The channel with the lowest frequency covers the plasma center as indicated by the spatial width of emission line, thus the measurements from this ECE channel are expected to show strong couplings with measurements originating from the plasma center. This is due to the relativistic downshift of the ECE from hot electrons in the plasma center which at the plasma edge (low density and low T_e) is not well reabsorbed. This effect also compromises the measurements from ECE channel #2 but at a shorter extent. Because of this, the measurements from these channels
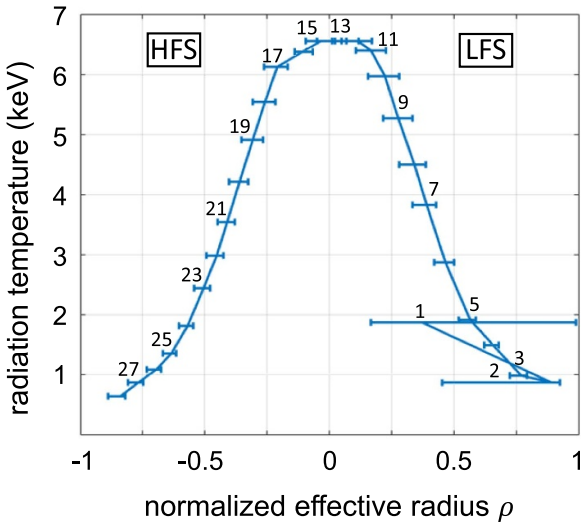
Figure 4. Radiation temperature profile calculated through the ray-tracing code TRAVIS from electron cyclotron emission measurements in W7-X plasma discharge 20160309.22 from $t = 0.30$ s to $t = 0.32$ s for the X-mode. Positive values of ρ represent radial regions near the low-field side (LFS) and negative, near the high-field side (HFS).

cannot be interpreted as localized temperature measurement. Thus, the radial positions of this channel will be obtained from the cold resonance, that is, neglecting kinetic effects such as relativistic.

Now, the coupling of one selected channel (#5 at about $\rho = 0.55$ in figure 4) is examined. Figure 5(a) shows the absolute value of the linear correlation (PPMC—solid gray lines), MI (broken red lines), PMI (solid red lines) and TE (dotted red lines) results. The instantaneous coupling with each individual channel is displayed as indicated in the title text of the figure. The channels are allocated spatially according to the normalized effective radius as shown in figure 4. The blue shaded areas represent the region where the radiation measured through channel #5 comes from and its mirrored location on the opposite field side.

Clear peak structures are identified in all coupling calculations. Moreover, indications for couplings are seen in adjacent channels to #5 as well. The most prominent peak, however, is found in the opposite field side at channel #23, close to the mirrored effective radius location of channel #5 but shifted to the low-field side. Also, the radial region covered by channel #23 (red shaded area) overlaps with the mirrored location of the reference channel. At this point, one may conclude that the flux surface is identified within the resolution of the coupling analysis. The broad peak structure around channel #23 indicates radial couplings with neighboring channels. This is, not sharply pinpointing one specific channel, but rather a radial location with a specific width (as seen from the radial overlaps seen in figure 4). A more detailed inspection shows that besides identifying a coupling structure near the suggested position of the flux surface, linear correlation indicates couplings with the channels in the low-field side closest to the ECE

horn antenna, adjacent channels and other channels sensitive also to radiation coming from the plasma center.

For the analysis of linear dependencies, only the linear correlation is implemented given that the fluctuations through these surfaces are quickly enough leveled off, for a synchronous analysis to be representative. It is noted that the linear correlation indicates coupling with channels in the core but also even further out the dominant peak ($\rho \sim -0.75$). The linear correlation is now compared to the MI which takes also non-linear dependencies into account. The comparison with noise levels provides the 'detection' limit as shown by the gray shaded area in figure 5(a). The MI indicates coupling structures similar to the linear correlation but exhibit differences to the linear correlation as well. Considering the significance threshold, some couplings suggested by the linear correlation are not significant in the MI analysis.

Next, we study the MI discounted from information in other channels. The PMI was calculated systematically discounting for all other ECE channels. The largest impact was found if channel #16 (the heating channel) was discounted for. The PMI (conditional on the signal from channel #16) shows one prominent coupling peak above the significance level on the $\rho < 0$ part of the profile. Moreover, spatial coupling structures are quite narrow compared to the linear correlation and less coupling indications above the significance threshold are found compared to the linear correlation and MI. Additional coupling indications for more outside lying channels (#1, #2) for negative ρ agree with the outcome of the radiation transport calculations (as indicated by the overlap of spatial widths of emission lines shown in figure 4). This is, through neglecting the characteristics contained in the signal measured from the heating channel that seem to influence the pairwise couplings.

Comparing the results from the PMI analysis with the TE $T_{\#5 \to \#X}$ ($k = 1$, cf section 2) analysis, results in a similar coupling structure near the expected flux surface location. In the TE analysis, the peak structure is narrower and as low in amplitude as the detection limit.

Performing the same coupling analysis for ECE channel #23 as the reference (figure 5(b)) results in similar results. The individual peaks of the coupling structure in the opposite field side of the reference channel lies for all methods at the same radial location. This finding is providing evidence that the ECE line of sight transverses the flux surface twice (see also figure 6). Taking the width of the peaks, a comparison with ECE profiles from ray-tracing (with TRAVIS using a VMEC equilibrium), indicates that the position of the flux surface is consistently detected. A small radial shift of the peak maximum, however, occurs systematically toward the high-field side. The shift is about 1 GHz (corresponds to one channel number, cf section 3.1) and coincides with the asymmetric (high-field side shift) broadening of the ECE emission layer by hot electrons. The typical scale of the shift $\frac{\Delta \nu}{\nu} \sim \frac{T_e}{m_e c^2}$ [29] corresponds to our observations.

Between the synchronous nondirected coupling analysis methods (PPMC, MI and PMI analysis), the clearest indication for flux surface coupling is found in PMI calculations conditional on the signal from the heating channel. This finding is

(a) (b)
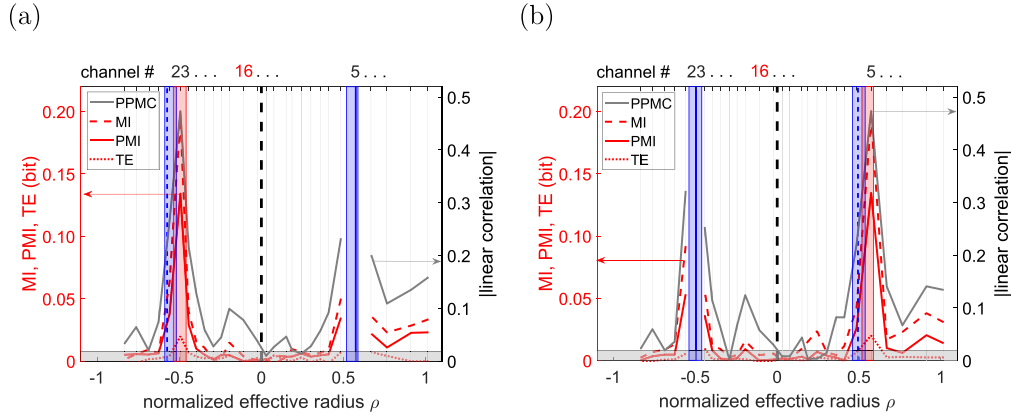
Figure 5. (a) Absolute value of the Pearson product-moment correlation (PPMC), mutual information (MI), partial mutual information (PMI) and transfer entropy (TE) $T_{\#5 \to \#X}$ of the ECE radiometer channel #5 with all others for ECE signal in W7-X plasma discharge 20160309.22 from $t = 0.30$ s to $t = 0.32$ s. Channel #16 is discounted in the PMI analysis and the sample shift for the TE analysis is $k = 1$. The blue solid line indicates the radial position of the reference channel and the blue dashed line illustrates the equivalent position in the opposite field side of channel #5. The blue shaded areas indicate the radial region covered from ECE channel #5 and its mirrored location. The gray shaded area reflects the significance threshold for the information quantities. The red shaded area indicates the location from channel #23. (b) Identical analysis for channel #23 as the reference.

interpreted to reflect the impact of spurious signals correlated with a central channel affected by the ECRH.

In a next step, the PMI coupling analysis method is extended to more ECE channels as the reference (#4, #5 and #6), which results in similar outcomes (figure 6). For a better visualization of the physical significance of the results, figure 6(a) shows a poloidal cross section of W7-X with a Poincaré plot depicting the line of sight of the ECE diagnostic crossing the plasma center, as well as the locations of the three ECE reference channels and the flux surfaces connecting these to their respective locations in the opposite field side. The results of the PMI analysis discounting again, the influence of the heating channel on the mutual dependencies between the reference channel and all others, are shown in figure 6(b). Similar to the results shown in figure 5(a), couplings with adjacent ECE channels appear, as well as peak structures near the respective flux surface position in the opposite magnetic field side indicated by TRAVIS.

As the reference channel moves inwards, closer to the plasma center, so do the PMI coupling structures. Couplings between reference channels $\#4 - 5$ and the two outermost channels can be seen. This can be retraced from the spatial widths of emission lines in the temperature profile (figure 4) due to relativistically downshifted emission from hot core electrons. However, even when PMI analysis offers the most robust results out of the other methods, not yet understood couplings with channels measuring radiation from the high temperature gradient ($\#8 - 11$) are observed. Nevertheless, the spatio-temporal coupling analysis of ECE data for these three ECE signal channels as the references identify the position of the respective flux surfaces in the opposite field side. However, the shift of the coupling structure to the low-field side observed from figure 5 prevails.

Besides the results during the 'high' power phase ($t = 0.30$ s), coupling analysis during the 'low' and 'medium' power phases were also carried out confirming the reported

results from the high-power phase. With increasing heating power the coupling strengths also increase, the identifiable flux surfaces lie closer to the plasma edge, the mismatch between the calculated positions of the flux surfaces and the ones suggested by the coupling analysis increases, and more in number coupling structures appear across all coupling analysis methods. Throughout the three different power phases during this plasma discharge, the determination of the position of the flux surface in the opposite field side of a reference channel was possible.

A different case to reveal the capabilities of the PMI technique is reflected in figure 7. Here, we show the MI (no discounting), the PMI (discounting system noise) and the PMI discounting for an ECE channel adjacent to the chosen reference (channel #9 indicated by the black dotted line and discounted channel #10 red dotted line, respectively). A Fourier analysis of the scrutinized channels indicates typical frequencies of about 4 kHz allowing one to classify the observed fluctuations as MHD mode activity. The coupling analysis is omitted for ECE channels with low signal-to-noise ratio.

It is clearly seen that the coupling is localized in the core ($|\rho| < 0.5$). The system noise is discounted by conditioning on a time window of the ECE channel after plasma operation (dashed black line in the figure). The small difference of MI (gray) and PMI (black) confirms the coupling to result from plasma effects. Finally, the PMI conditioned on a channel within the MHD-mode activity region indicates significantly lower coupling. We recall that (this specifically conditioned) PMI $I(X_{\text{ref}}, Y_i | X_{i=10})$, indicated by the red dotted line, could be seen as a measure of how much information is left in an ECE channel Y_i to predict time series from the reference channel X_{ref} (if X_{ref} is known). In other words, the red curve reveals how much new information comes from the respective location in addition to channel #10. The large decrease (red vs. gray) indicates a close coupling in channels #9 and #10 (red)
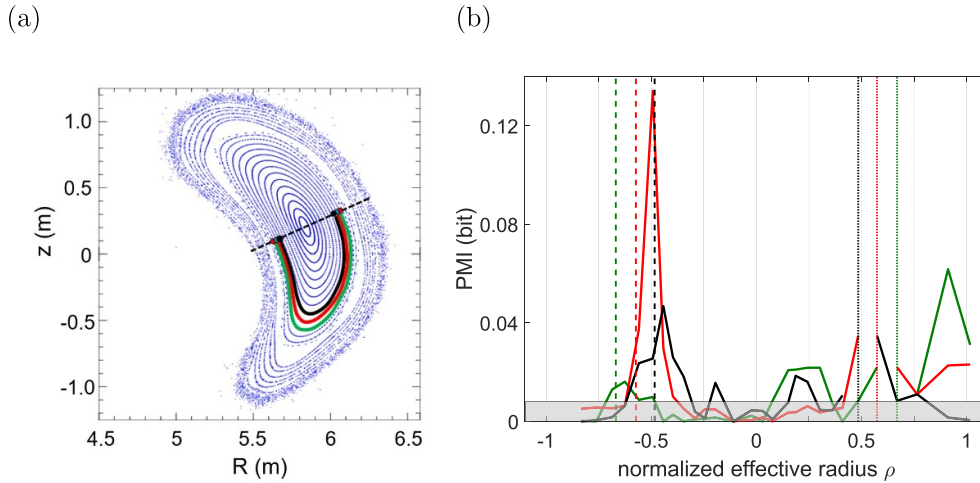
Figure 6. (a) Poloidal cross section with a Poincaré plot of the magnetic configuration implemented in plasma discharge 20160309.22 for a toroidal angle $\phi = 6.1$ ° at W7-X. Black dashed line depicts the line of sight of the ECE diagnostic. Green, red and black curves and markers indicate the flux surfaces connecting channels #4, #5 and #6 with their respective locations in the opposing field side. (b) Extended PMI analysis w.r.t. three different reference ECE channels mapped on the normalized effective radius ρ. Channel #16 is discounted in the PMI analysis. The gray shaded area reflects the significance threshold.
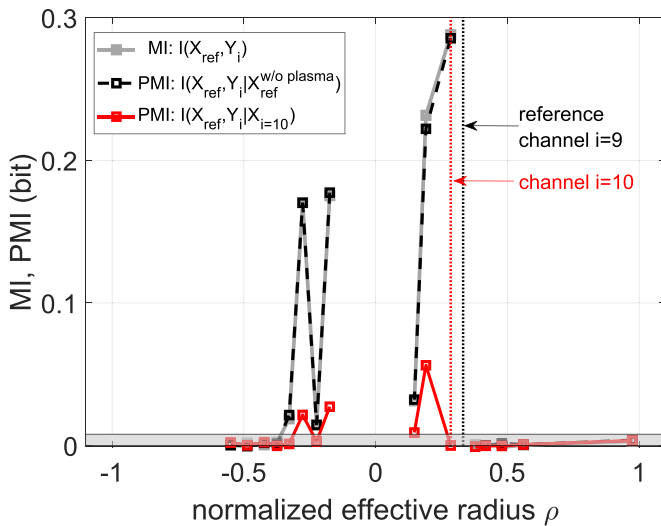
Figure 7. MI and PMI for MHD mode activity identification in the W7-X discharge 20180829.33 from $t = 1.00$ s to $t = 1.01$ s (mean density of 3×10^{19} m^{-3}, heated at 2 MW ECRH power). The coupling analysis of radiometer channel #9 (reference channel, $i = 9$) with all others channels is shown. The abscissa represents the position of the ECE emissivity determined by ray-tracing calculations. The gray shaded area indicates the significance threshold for the information quantities.

due to MHD mode activity. We thus conclude that the coupling involves regions $|\rho| \lesssim 0.3$, and thus has a global character. We note that the observed coupling disappears in the course of the discharge.

4. Discussion and conclusions

All investigated traditional and information-based coupling analysis methods identify coupling of ECE radiometer channels. TE analysis results coincide with the results from the

other methods but appear to be less sensible for the conducted coupling analysis. PMI analysis, with its capability to discount for specific spurious signals (stemming from different noise sources), is able to extract T_e-fluctuations from the background of other fluctuating signal components. As a result, PMI delivers clearer results than linear correlation and MI analysis for the specific data set analyzed in this paper. Detailed assessments of cross-talk effects and common noise sources from amplifiers and detection electronic groups are giving valuable input from structural similarities in the PMI analysis.

While the indication of coupling on flux surfaces is interpreted to be due to fluctuations carried by parallel transport on flux surfaces, the introduced analysis also provides indications for couplings perpendicular to flux surfaces as reported in [9]. The broadening of the coupling structures, moreover, may provide insight into energy and particle transport but is also found to be affected by apparent couplings due to induced noise and radiation transport. Moreover, the impact of the physics of ECE, here the asymmetric broadening due to relativistic mass increase, leads to systematic shifts of the coupling peak to apparently higher magnetic field positions.

All in all, the findings of spatial coupling analysis with PMI of ECE radiometer data confirm the position of the flux surfaces in plasma operation. We conclude that the method confirms (as expected) MHD equilibrium calculations. The experimental approach is simple and robust, since it relies on the coupling analysis method (PMI) of electron cyclotron emissivity fluctuations. The technique was also applied to reveal the spatial coupling and extent of MHD mode activity. The coupling analysis does not depend on the signal level or calibration of the ECE signal. Therefore, and by taking note that ECE is a microwave measurement [30], we expect that the method could be also employed to confirm the existence of flux surfaces in harsh environments.

As an overall conclusion, we find that conditional information coupling analysis may provide indications of physical

processes, e.g. parallel transport or spatial structures of fluctuations. Equally important, the coupling analysis also indicates how much the measurement process is affected by spurious signals. Therefore, through discerning between physically and not physically relevant contributions to the mutual dependencies between synchronous ECE measurements, the introduced method of PMI analysis appears to provide an added value for the analysis of experimental fluctuation data from fusion plasmas.

Acknowledgments

ORCID iDs

J F Guerrero Arnaiz https://orcid.org/0000-0002-7650-2918

A Dinklage https://orcid.org/0000-0002-5815-8463

J Geiger https://orcid.org/0000-0003-4268-7480

M Hirsch https://orcid.org/0000-0002-7120-6087

U Höfel https://orcid.org/0000-0003-0971-5937

N Marushchenko https://orcid.org/0000-0002-0415-1303

R C Wolf https://orcid.org/0000-0002-2606-5289

References

[1] Nührenberg J and Zille R 1986 Stable stellarators with medium β and aspect ratio *Phys. Lett.* A **114** 129
[2] Grieger G, Lotz W and Merkel P *et al* 1992 Physics optimization of stellarators *Phys. Fluids* B **4** 2081
[3] Wolf R C *et al* 2017 Major results from the first plasma campaign of the Wendelstein 7-X stellarator *Nucl. Fusion* **57** 102020
[4] Wagner F and Wobig H 2005 Magnetic confinement *Plasma Physics: Confinement, Transport and Collective Effects* eds A Dinklage, T Klinger, G Marx and L Schweikhard (Berlin: Springer) pp 375–97
[5] Pedersen T *et al* 2015 Plans for the first plasma operation of Wendelstein 7-X *Nucl. Fusion* **55** 126001
[6] Frenzel S and Pompe B 2007 Partial mutual information for coupling analysis of multivariate time series *Phys. Rev. Lett.* **99** 204101
[7] Staniek M and Lehnertz K 2008 Symbolic transfer entropy *Phys. Rev. Lett.* **100** 158101
[8] Runge J, Heitzig J and Marwan N *et al* 2012 Quantifying causal coupling strength: A lag-specific measure for multivariate time series related to transfer entropy *Phys. Rev.* E **86** 061121
[9] van Milligen B, Höfel U and Nicolau J *et al* 2018 Study of radial heat transport in W7-X using the transfer entropy *Nucl. Fusion* **58** 076002

[10] James R, Barnett N and Crutchfield J 2015 Information flows? A critique of transfer entropies *Phys. Rev. Lett.* **116** 238701
[11] Smirnov D A 2013 Spurious causalities with transfer entropy *Phys. Rev.* E **87** 042917
[12] Schreiber T 2000 Measuring information transfer *Phys. Rev. Lett.* **85** 461
[13] Murari A, Lungaroni M and Peluso E *et al* 2018 On the use of transfer entropy to investigate the time horizon of causal influences between signals *Entropy* **20** 627
[14] van Milligen B, Höfel U and Hirsch M *et al* 2017 The impact of heating power on radial heat transport in W7-X *Nucl. Fusion* **57** 056028
[15] Nicolau J H, Garcia L and Carreras B A *et al* 2018 Applicability of transfer entropy for the calculation of effective diffusivity in heat transport *Phys. Plasma* **25** 102304
[16] Boltzmann L 1877 Über die beziehung zwischen dem zweiten hauptsatz der mechanischen wärmetheorie und der wahrscheinlichkeitsrechnung resp. den sätzen über das wärmegleichgewicht *Sitzb. Kais. Akad. Wiss. Wien Math. Naturwiss. Cl.* **76** 373
[17] Marinescu D C and Marinescu G M 2012 Chapter 3 - classical and quantum information theory *Classical and Quantum Information* eds Marinescu D C and Marinescu G M (New York: Academic) pp 221–344
[18] Garbet X, Dubuit N and Asp E *et al* 2005 Turbulent fluxes and entropy production rate *Phys. Plasmas* **12** 082511
[19] Shannon C E 1948 A mathematical theory of communication *Bell Syst. Tech.* J. **27** 379
[20] Ware B M W and Ferron J 2013 Describing the relationship between two quantitative variables: correlation *Introductory Statistics: A Conceptual Approach Using R* (New York: Routledge)
[21] Marushchenko N, Turkin Y and Maassberg H 2014 Ray-tracing code TRAVIS for ECR heating, EC current drive and ECE diagnostic *Comput. Phys. Commun.* **185** 165
[22] Hartfuss H J, Geist T and Hirsch M 1997 Heterodyne methods in millimetre wave plasma diagnostics with applications to ECE, interferometry and reflectometry *Plasma Phys. Control. Fusion* **39** 1693
[23] Höfel U, Hirsch M and Kwak S *et al* 2019 Bayesian modeling of microwave radiometer calibration on the example of the Wendelstein 7-X electron cyclotron emission diagnostic *Rev. Sci. Instrum.* **90** 043502
[24] Schmuck S, Hartfuss H J and Hirsch M *et al* 2009 Design of the ECE diagnostic at wendelstein 7-X *Fusion Eng. Des.* **84** 1739
[25] Hirsch M and Höfel U *et al* 2019 ECE diagnostic for the initial operation of Wendelstein 7-X *EPJ Conf.* p 03007
[26] Hirshman S, van Rij W and Merkel P 1986 Three-dimensional free boundary calculations using a spectral green's function method *Comput. Phys. Commun.* **43** 143
[27] Yokoyama M *et al* 2007 Core electron-root confinement (CERC) in helical plasmas *Nucl. Fusion* **47** 1213
[28] Dinklage A, Beidler C and Helander P *et al* 2018 Magnetic configuration effects on the Wendelstein 7-X stellarator *Nat. Phys.* **14** 855
[29] Hutchinson I H 2002 Chapter 5 *Principles of Plasma Diagnostics* (Cambridge: Cambridge University Press) pp 158–66
[30] Biel W *et al* 2015 Demo diagnostics and burn control *Fusion Eng. Des.* **96–97** 8